

## Article

# Spatiotemporal Heterogeneity of Precipitable Water Diurnal Variation over the Tibetan Plateau Based on a Refined 2D Water Vapor Reconstruction

Hongjun Li <sup>1,\*</sup>, Zhengjun Hou <sup>2</sup>  and Zhuangen Qin <sup>1</sup>

<sup>1</sup> China Anergy Group Third Engineering Bureau Co., Ltd., Chengdu 610036, China; qinzhuangen9397@sina.com

<sup>2</sup> Chengdu Sunvison Intelligent Technology Co., Ltd., Chengdu 610065, China; houzj9@sina.com

\* Correspondence: lihj09@sina.com

**Abstract:** Atmospheric water vapor is a critical factor influencing rainfall, snowfall, and avalanche occurrences, with its diurnal variations providing key insights into such phenomena. However, in high-altitude mountainous areas, the spatial and temporal resolution of water vapor products is insufficient to depict their diurnal variation characteristics. This study aimed to refine the understanding of diurnal Precipitable Water Vapor (PWV) variations using the ANUSPLIN to obtain a two-dimensional water vapor field with a resolution of  $0.1^\circ \times 0.1^\circ$  during the monsoon period from 2007 to 2015, which was verified based on ground-based GPS water vapor observations. The findings reveal that incorporating China Meteorological Forcing Data (CMFD) greatly enhances the diurnal variation patterns of PWV, resulting in the appearance of extreme values of PWV daily variation about three hours later than the MERRA reanalysis. In the southern Tibetan Plateau (TP), the diurnal variation of PWV is closer to GPS PWV in terms of amplitude and phase. Spatially, PWV variations are weaker in the central TP but stronger in other regions, particularly during the mid-monsoon period (July–August). Temporally, the central TP experiences maximum PWV from nighttime to early morning (18:00–4:00 UTC), while the surrounding southern and northern areas peak from afternoon to evening (8:00–12:00 UTC), approximately three hours earlier than precipitation peaks. Temporally, the central Tibetan Plateau experiences maximum PWV from nighttime to early morning (18:00–4:00 UTC), while the surrounding southern and northern areas peak from afternoon to evening (8:00–12:00 UTC), approximately three hours earlier than precipitation peaks.

**Keywords:** precipitable water vapor (PWV); ANUSPLIN; GPS retrievals; Tibetan Plateau (TP); diurnal variation



Academic Editor: Yoshihiro Tomikawa

Received: 26 November 2024

Revised: 17 January 2025

Accepted: 18 January 2025

Published: 27 January 2025

**Citation:** Li, H.; Hou, Z.; Qin, Z. Spatiotemporal Heterogeneity of Precipitable Water Diurnal Variation over the Tibetan Plateau Based on a Refined 2D Water Vapor Reconstruction. *Atmosphere* **2025**, *16*, 139. <https://doi.org/10.3390/atmos16020139>

**Copyright:** © 2025 by the authors. Licensee MDPI, Basel, Switzerland. This article is an open access article distributed under the terms and conditions of the Creative Commons Attribution (CC BY) license (<https://creativecommons.org/licenses/by/4.0/>).

## 1. Introduction

The increase in heavy rainfall and heavy snowfall from afternoon to night enlarges the risk of avalanches and also heightens the difficulty of emergency response for mountain disasters like avalanches. Therefore, understanding the formation mechanism of diurnal precipitation variation and improving its forecast accuracy is extremely urgent. Among them, the distribution characteristics of atmospheric precipitable water play a crucial role. The diurnal variation of water vapor usually shows that in the daytime, the higher temperature leads to an increase in near-surface water vapor due to processes like surface evaporation and water vapor transport. When the temperature drops low enough, the water vapor will condense into ice crystals or snowflakes. In mountainous areas, the increase in

water vapor in the afternoon and the arrival of cold air at night cause rapid condensation of water vapor, and the snowfall may increase rapidly in a short time. Meanwhile, the increase in water vapor in the daytime makes the humidity of new snow increase, and the new snow accumulates on the original snow layer under the action of gravity. When the temperature drops at night, the snow freezes. Such repeated processes lead to changes in the snow layer structure, reducing the cohesion between the snow layers and worsening the stability. A rapid increase in water vapor can change the humidity and density of the snow, forming fragile or weakly bonded layers. For example, in the “11·7” avalanche in 2023, the atmospheric water vapor content in the southeastern Tibetan Plateau increased rapidly and reached saturation one week in advance, with accumulated snowfall from multiple snow events, ultimately triggering the avalanche under the action of gravity.

Most of the previous studies related to water vapor have relied on water vapor products from satellites (such as MODIS, AIRS, etc.) and reanalysis data (such as NVAPOR, MERRA, ERA interim, JRA 55, NCEP final, etc.). However, the accuracy of these products varies with different regions [1–3]. For instance, Lu et al. (2015) evaluated the MODIS near-infrared water vapor products in the TP region using JICA GPS data and found that the accuracy of the MODIS near-infrared products was relatively high under clear-sky conditions, but they were slightly overestimated (by 6–20%) [4]. Zhao et al. (2015) highlighted regional biases in reanalysis datasets, noting underestimations of 20–40% in western China and as much as 60% in the southwestern TP [5]. These errors are attributed to complex terrain, sparse-sounding stations, and insufficient data for validation. Reanalysis datasets also struggle to capture interannual variations in precipitable water in the TP [6], while satellite products often suffer from many missing data points due to local convection and clouds. Additionally, most of the global models used for reanalysis data have a relatively low resolution and are unable to accurately describe the physical processes related to the complex terrain of the plateau. Therefore, currently, most of the data are unable to describe the multi-scale characteristics of water vapor. It is imperative to develop a high-resolution dataset tailored to the TP to better analyze the spatiotemporal distribution patterns of atmospheric water vapor.

Water vapor exhibits a strong dependence on altitude, with the TP characterized by the lowest column water vapor content in China, which decreases from southeast to northwest [7]. Spatially, the total column water vapor peaks in the northeastern TP and exhibits contrasting trends south and north of the Tanggula mountains [8–10]. Seasonal variations are also evident, with monsoon-period water vapor several times higher than that during non-monsoon periods [8,11,12]. In recent decades, the water cycle system in the TP has undergone significant changes: the melting of glaciers has intensified, and the thickness of the active layer in the permafrost area has increased (Tibet Regional Innovation Cluster, 2015); lakes south of the Yarlung Zangbo River have shrunk, while those north of the river have expanded significantly [13]; snowfall in the Himalayan Mountains has decreased [14]; precipitation in the southern and eastern parts of the plateau has decreased [15], while convective precipitation in the central part has increased [16]; water vapor in the central and northern parts of the plateau has increased, while that in the southern part has decreased [4]. Meanwhile, the surface wind speed on the plateau has weakened, which has also weakened the water vapor exchange between the TP and its surrounding areas [17–19].

The diurnal variation of water vapor is a critical yet underexplored phenomenon on the TP. Under the background of large-scale circulation, the combined effects of solar radiation, local circulation, surface evaporation, diurnal variation of precipitation, and thermal differences of different surface states result in an obvious diurnal variation process of water vapor on the plateau [20–22]. Meanwhile, the topography also affects the diurnal variation characteristics of water vapor and its transport process [23]. Based on the observations from

existing GPS stations, it has been found that the peak value of the total column water vapor on the plateau usually appears at night, and the trough value appears in the morning [24], which is closely related to the fact that most of the precipitation on the plateau occurs from evening to night [25]. Some studies have also found that the atmospheric water vapor in the Lhasa River Valley is the lowest from 14:00 to 16:00 LST and the highest from 21:00 to 00:00 LST, mainly controlled by local circulation systems such as valley winds [26]. During the passage of a weather system, the water vapor transport on the southern slope of the eastern section of the Himalayas is relatively strong from afternoon to night, and the transport height can reach 5500 m, while in the morning, the water vapor can only be transported from the foot of the mountain to the position below 4000 m above sea level [27]. The influence of the monsoon system on the diurnal variation of water vapor on the plateau cannot be ignored. The diurnal variation of water vapor before the monsoon outbreak is more significant than that during the monsoon period, especially in the central part of the plateau [23]. In addition, climate warming has intensified the thermal differences between high-altitude and low-altitude areas and strengthened the boundary mixing, thus affecting the diurnal variations of wind fields and water vapor fields in alpine regions [28]. Despite recent progress, gaps remain in capturing the fine-scale spatial and temporal characteristics of water vapor over the TP. Existing datasets lack the resolution to depict diurnal variations accurately, particularly during critical pre-monsoon and monsoon periods. Furthermore, the role of local factors, such as terrain and microclimates, in modulating water vapor dynamics remains insufficiently studied. This study addressed these gaps by constructing high-resolution ( $0.1^\circ \times 0.1^\circ$ ) water vapor datasets for the TP using the ANUSPLIN interpolation technique, validated against ground-based GPS retrievals. Our research provides novel insights into the spatial and temporal characteristics of water vapor, with a specific focus on diurnal variations during pre-monsoon and monsoon periods. By highlighting regional differences in water vapor dynamics and their implications for precipitation and hydrological processes, this study contributes to a deeper understanding of atmospheric processes over high-altitude regions and offers valuable data for climate modeling and disaster risk management.

## 2. Data and Methodology

### 2.1. MERRA

MERRA (Modern-Era Retrospective Analysis for Research and Applications, Version 2) is a long time-series atmospheric reanalysis dataset produced by NASA's Global Modeling and Assimilation Office (GMAO). The data have been available since 1980 and cover the whole globe. They include various meteorological variables like net radiation, temperature, relative humidity, wind speed, turbulent evapotranspiration, cloud top pressure, cloud top temperature, sea level pressure, total precipitable water vapor, etc. It has a spatial resolution of about 50 km ( $\sim 0.5^\circ \times 0.625^\circ$ ) and a temporal resolution of 1 h [29].

### 2.2. GPS Observations

In this study, the precipitable water vapor retrieved from GPS was used to evaluate the reconstructed dataset after downscaling. Moreover, observations from nine GPS stations distributed between  $82^\circ\text{E}$  and  $95^\circ\text{E}$  were used. The precipitable water vapor throughout the entire atmospheric layer was retrieved by taking advantage of the signal delays of these GPS stations in the atmosphere. All of these stations are located at an altitude of 4200 m. For detailed information about the nine stations, please refer to Wang et al. (2017) [30]. The precipitable water vapor (PWV) data during the monsoon period (from May to September) from 2007 to 2013 were obtained, with a temporal resolution of one hour. Due to differences in the establishment time of stations and observational conditions, etc., there are certain

variations in the number of valid samples for calculating the precipitable water among different stations. The average PWV of each station during the monsoon period ranges from 6.8 mm to 11.4 mm, while the average PWV during the summer season (from June to August) is from 8.5 mm to 13.6 mm.

### 2.3. CMFD

The China Meteorological Forcing Dataset (CMFD) is a near-surface meteorological dataset with high spatial and temporal resolutions, specifically developed for land surface process research in China [31]. It is generated by integrating remote sensing products, reanalysis datasets, and on-site observational data from meteorological stations. This multi-source data integration approach can combine the advantages of different data sources to enhance the accuracy and reliability of the dataset. It starts from January 1979 and has been continuously updated, and it includes seven near-surface meteorological elements such as 2 m air temperature, surface air pressure, specific humidity, 10 m wind speed, downward shortwave radiation, downward longwave radiation, and precipitation rate. Moreover, its spatial and temporal resolution is  $0.1^\circ$  and 3 h, respectively.

### 2.4. ANU-SPLIN Downscaling Method

Currently, downscaling mainly includes dynamical downscaling (such as regional climate models) and statistical downscaling (primarily based on the correlative relationships established among meteorological variables in different regions) methods. The dynamical downscaling method, like WRF, has a strong physical mechanism. It could simulate atmospheric dynamics and physical processes to capture spatial and temporal variations effectively. However, their accuracy is limited by uncertainties in initial conditions and complex terrains, with the increase in resolution controlling and limiting the uncertainties within its grids having become the main issue of the current downscaling methods, and they require substantial computational resources [32]. In addition, a statistical method like quantile mapping improves the consistency between observed and simulated data, particularly for precipitation and temperature. However, it neglects physical processes, limiting its accuracy in extreme climate events and complex terrains [33]. The multivariate thin-plate smoothing spline data interpolation software ANUSPLIN (<https://support.climateengine.org/article/48-anusplin>, accessed on 25 November 2024), developed by the Australian National University, is a rapid and simple spline function interpolation method, which is often used for downscaling processing of atmospheric precipitation, temperature, and other variables [34,35]. ANUSPLIN can perform spatial interpolation on variables based on multiple influencing factors simultaneously. It is often used for downscaling meteorological elements such as precipitation and temperature and also has good applications in other fields, such as geography, hydrology, and meteorology. Compared with interpolation methods such as the inverse distance interpolation method, ordinary kriging method, cokriging method, and empirical Bayesian kriging (EBK), the interpolation results of ANUSPLIN can provide better spatial distribution and lower errors [36].

In this study, taking the MERRA precipitable water vapor (PWV) as the background field, based on the  $0.1^\circ$  grid point altitude, surface air pressure, 2 m air temperature above the surface, and 2 m specific humidity variables from the China Meteorological Forcing Dataset (CMFD), with longitude and latitude (in radians) as the independent spline variables, and simultaneously taking the topographic altitude ( $H$ , in meters), surface air pressure ( $P$ , in hPa), 2 m air temperature above the surface ( $T$ , in K), and 2 m specific humidity above the surface ( $Q$ , in  $\text{g} \cdot \text{Kg}^{-1}$ ) as the covariates, the ANUSPLIN interpolation method was utilized to downscale the MERRA data, with a resolution of  $0.5^\circ \times 0.67^\circ$ ,

during the monsoon period (May–September) from 2007 to 2015, thereby obtaining a precipitable water vapor field with a resolution of  $0.1^\circ \times 0.1^\circ$  and a temporal resolution of three hours. Verification and analysis were then conducted based on the GPS water vapor observations during the monsoon period from 2007 to 2013. When generating the fitting surface, the thin-plate spline smoothing function model used by ANUSPLIN is shown in Formula (1):

$$Z_i = f(x_i) + b^T y_i + e_i \quad (i = 1, \dots, N), \tag{1}$$

where  $x_i$  is the independent spline variable;  $f$  is the smoothing function with respect to  $x_i$ ;  $y_i$  is the independent covariate;  $e_i$  is the independent zero-mean error term;  $N$  is the number of spatial points;  $b$  is the coefficient of  $y_i$ ; and  $Z_i$  is the dependent variable at the  $i^{\text{th}}$  spatial point.

The least squares method was employed to select the most appropriate fitting function  $f$  and covariate coefficient  $b$ , and the Generalized Cross-Validation (GCV) [37,38] was used to optimize the parameters of the fitting surface. Due to the resolution of the MERRA input variables being  $0.5^\circ \times 0.67^\circ$ , within the plateau region, the number of input sample points did not exceed 2000. Therefore, the SPLINA module was used in this section to calculate the fitting surface. Since PWV is exponentially correlated with covariates such as altitude, a natural logarithm transformation was first applied to PWV before fitting. This transformation can reduce the skewness of the data and the roughness of the fitting surface.

### 2.5. Diurnal Variation Analysis Based on Fourier Transform

In this study, the downscaled PWV field averaged over the seven years from 2007 to 2013 was standardized first. Then, the Fourier transform was performed on the standardized PWV, and the spatial distribution of its diurnal variation was analyzed, as shown in Formula (2).

$$PWV_s = \frac{PWV_i - \overline{PWV}}{\sqrt{\frac{1}{M} \sum_i^M (PWV_i - \overline{PWV})^2}} \tag{2}$$

$$PWV_s(t') = PWV_{s0} + \sum_{n=1}^N (A_n \sin(nt' + \sigma_n)) + R \tag{3}$$

Here,  $PWV_i$  represents the precipitable water vapor at each time, and its unit is mm;  $PWV_s$  represents the standardized precipitable water vapor value within a single grid and is dimensionless;  $PWV_{s0}$  is the average value of  $PWV_s$ ;  $R$  is the residual;  $A_n$  represents the amplitude of each harmonic;  $\sigma_n$  represents the phase of each harmonic;  $M$  is the number of samples; and  $N$  is the number of harmonics.

Since the time resolution after downscaling is three hours, in this section, the harmonics with a period of  $8 \times 3$  hr are analyzed, corresponding to  $t' = \frac{2\pi t}{8}$  in Formula (3), in which  $t' = 1, 2, \dots, 8$ , corresponds to 00:00 UTC, 03:00 UTC, 06:00 UTC, 09:00 UTC, 12:00 UTC, 15:00 UTC, 18:00 UTC, and 21:00 UTC, respectively.

### 2.6. Verification Method and Parameters

In this study, to ensure the reliability and accuracy of the high-resolution PWV developed for the TP, a rigorous validation process was conducted using ground-based GPS retrievals as a reference. The verification focused on key statistical metrics, including the correlation coefficient ( $R$ ), root mean square error ( $RMSE$ ), and mean bias, as follows:

$$R = \sum_{i=1}^n \frac{(x_i - \bar{x})(y_i - \bar{y})}{\sqrt{\sum_{i=1}^n (x_i - \bar{x})^2 \sum_{i=1}^n (y_i - \bar{y})^2}}, \tag{4}$$

where  $n$  is the number of data points;  $x_i$  is the observed GPS PWV values;  $y_i$  is the downscaled PWV values;  $\bar{x}$  is the mean of GPS PWV; and  $\bar{y}$  is the mean of downscaled PWV.

The correlation coefficient ( $R$ ) measures the strength and direction of the linear relationship between observed GPS PWV values ( $x_i$ ) and downscaled PWV values ( $y_i$ ). RMSE quantifies the average magnitude of the error between GPS PWV values ( $x_i$ ) and downscaled PWV values ( $y_i$ ). Mean bias evaluates systematic error by calculating the average difference between GPS PWV values ( $x_i$ ) and downscaled PWV values ( $y_i$ ).

### 3. Results

#### 3.1. Evaluation of Reconstructed PWV

Before using ANUSPLIN for downscaling, the correlation coefficient between the MERRA PWV and GPS retrievals was only 0.71; the deviation was approximately  $-2.21$ ; and the root mean square error was 3.68 (Figure 1a). However, after interpolation, the correlation coefficient of the data increased significantly, while the deviation and the root mean square error decreased substantially (Figure 1c). In addition, it shows an obvious spatial gradient over the TP, gradually decreasing from the southeast to the northwest, as shown in Figure 1b. For the PWV field obtained by downscaling MERRA based on the ASTER DEM, the influence of altitude on PWV is more pronounced. Moreover, the bias between the downscaled PWV field and the GPS PWV observations from 2007 to 2013 is smaller, approximately 0.87 mm, and the root mean square error is also smaller, about 2.25 mm. This indicates that the PWV obtained based on the fitting surface is closer to the GPS observations than that directly derived from the altitude correction formula. However, the PWV field obtained after the adjustment of the surface air pressure ( $P$ ), surface air temperature ( $T$ ), and surface absolute humidity ( $Q$ ) by CMFD is on the lower side, as shown in Figure 1d. This might be due to the strong dependence of PWV on  $Q$ , and the absolute humidity ( $Q$ ) field in CMFD is much smaller than that in MERRA. Nevertheless, there was a significant adjustment in the diurnal variation of PWV.

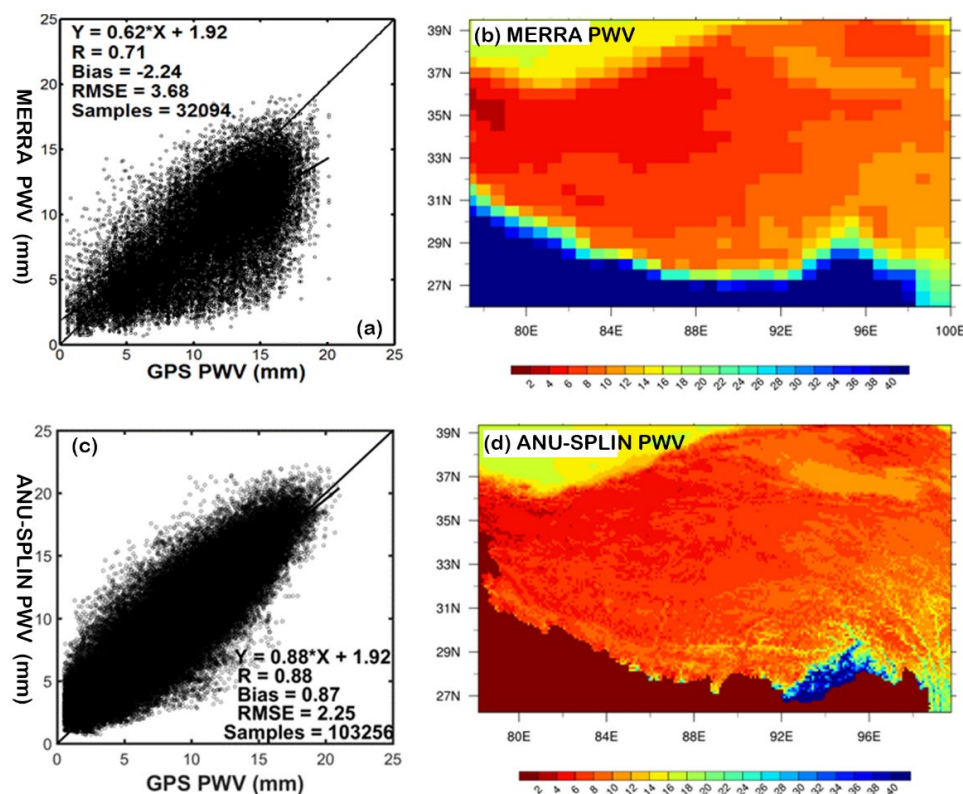


**Figure 1.** The MERRA (a,b) and ANUSPLIN downscaling PWV (c,d) spatial patterns (b,d) and their comparisons against the GPS PWV retrievals.

Since the ANUSPLIN downscaled PWV has a three-hour resolution, the corresponding local times each day are 00:00 LST, 03:00 LST, 06:00 LST, 09:00 LST, 12:00 LST, 15:00 LST, 18:00 LST, and 21:00 LST. Therefore, the GPS-retrieved PWV and MERRA PWV at the corresponding times are selected for diurnal variation analysis, as shown in Figure 2. In comparison to the diurnal variation of PWV observations at nine GPS stations distributed east and west of the Yarlung Zangbo River during the monsoon period from 2007 to 2013 (May to September), it was found that except for the CUIJ and JISG stations where the diurnal variation of PWV after downscaling is not significantly improved, at other stations, compared with MERRA, the description of the diurnal variation of PWV after downscaling has improved to varying degrees. Although the downscaled precipitable water vapor field still cannot well describe the “double-peak” diurnal variation state of PWV at the DANA, JIAW, and NCRS stations, there are slight improvements in its diurnal variation amplitude and phase. Compared with MERRA PWV, the diurnal variation of PWV after downscaling is significantly closer to the GPS observations at the CUOM, JRGR, and ZHXZ stations, and the diurnal variation amplitude and the time when the extreme values occur at the YARE station are also closer to the GPS observations. Especially at the JRGR station, the diurnal variation of PWV after ANUSPLIN interpolation is basically consistent with the GPS observations. This indicates that the addition of ITP-forcing surface air pressure, 2 m air temperature, and 2 m specific humidity variables has a significant adjustment on the diurnal variation of MERRA PWV. It not only improves the phenomenon of strong diurnal variation of precipitation to a certain extent but also makes the time when the peak and valley values of PWV diurnal variation closer to the GPS observations.

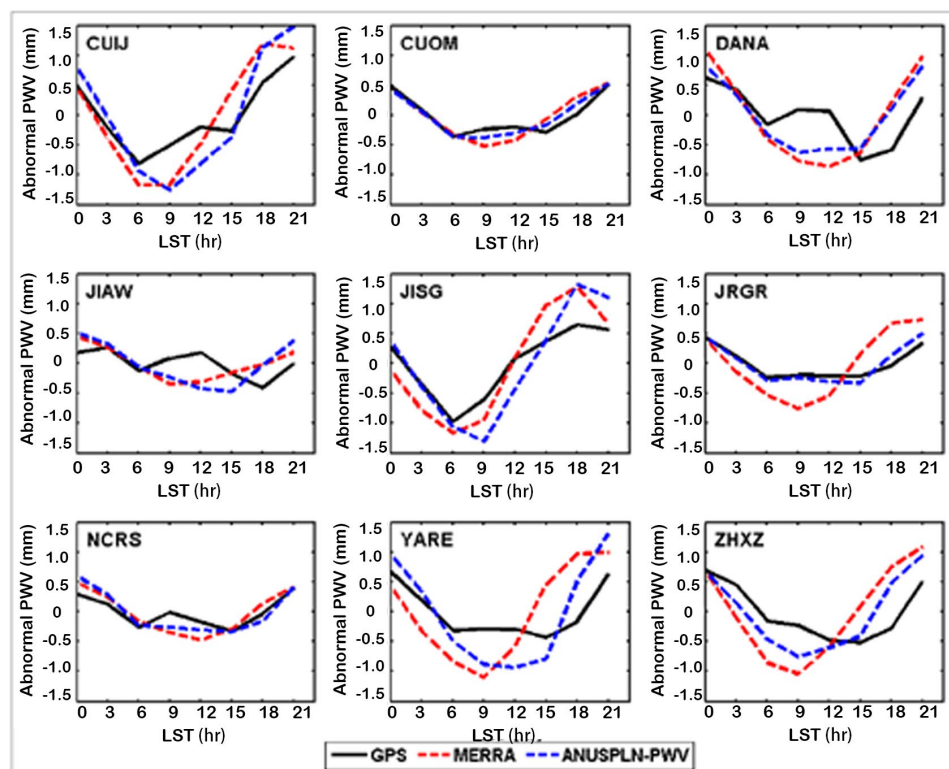


Figure 2. Comparison of PWV diurnal variations among the MERRA, ANUSPLIN, and GPS observations.

### 3.2. Spatial Features of PWV Diurnal Variation

The TP water vapor is transported eastward, and its diurnal variation also gradually spreads eastward, which has an important impact on the diurnal variation of the water cycle in East Asia. Bao et al. (2011) pointed out that the diurnal variation intensity and

propagation speed of small-scale systems (precipitation and water vapor) originating from the TP determine the diurnal variation characteristics of precipitation in the Meiyu Belt.

The amplitudes of the harmonics with a period of 24 hr are shown in Figure 3, corresponding to the spatial distributions of the PWV diurnal variation amplitudes in different stages of the monsoon.

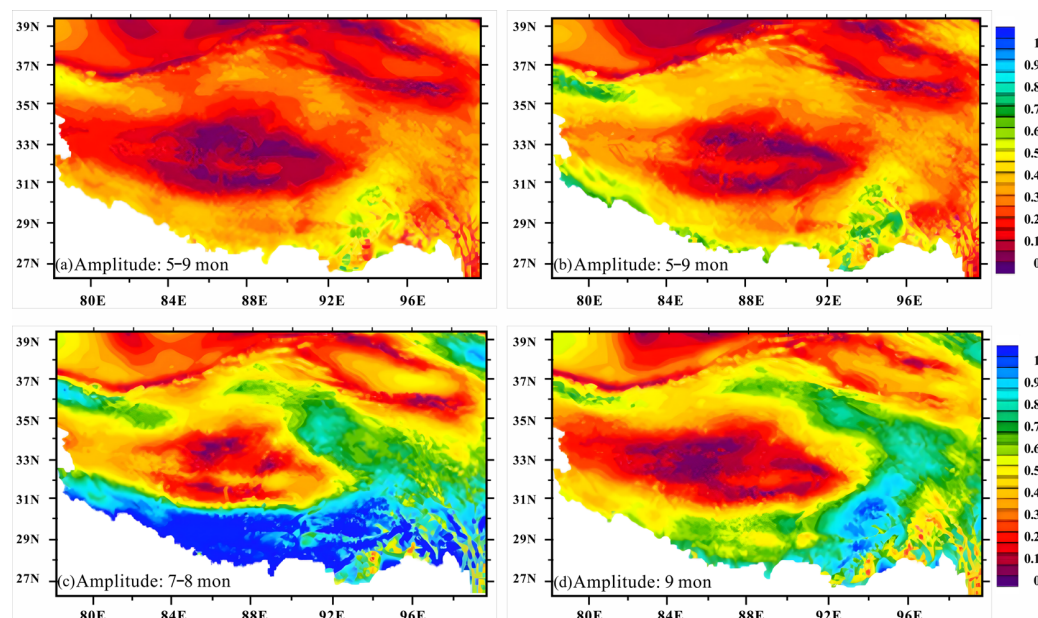


**Figure 3.** The Spatial Distribution of the Diurnal Variation Amplitude of ANUSPLIN downscaled PWV from 2007 to 2013. In panels, (a) May to September; (b) May to June, which is taken as the pre-monsoon period; (c) July to August, the mid-monsoon period; and (d) September, the post-monsoon period.

It is found that the diurnal variation of PWV is the weakest in the central TP, stronger in the border areas of the plateau, and the strongest in the southeastern part of the plateau. In the mid-monsoon and post-monsoon periods, the contrast in the diurnal variation of PWV between the plateau border and the central TP is more pronounced. The diurnal variation of PWV in the entire plateau region is stronger in the mid-monsoon period than in other periods. It is the weakest in the pre-monsoon period. Especially in the mid-monsoon period, the diurnal variation of PWV along the southern TP and the Himalayas is the strongest compared with other areas, which is consistent with the GPS station observations. This phenomenon indicates that the daily-scale water vapor transport in this area is relatively strong during the peak of the monsoon, implying that there are a large number of water vapor channels in the lofty Himalayas, allowing South Asian water vapor to enter the southern part of the TP.

In addition, it shows the times when the peaks of diurnal variation in precipitation PWV occur in different periods of the monsoon (Figure 4). It was found that the maximum value of the diurnal variation of PWV in the central part of the TP appears from midnight to morning (03:00–09:00 LST), while in the southern and northern peripheral areas, the maximum value appears earlier, from evening to midnight (18:00–00:00 LST), at least three hours earlier than in the central part. In southern TP, especially in the middle and western sections of the Himalayas, the diurnal variation of PWV is slightly later in the mid-monsoon period than in the other two periods. Moreover, in the mid-monsoon period, the central position of the diurnal variation of PWV in the TP is more to the west than in the other two periods, between 84–89°E, while in the pre-monsoon and post-monsoon periods, the central position is between 86–92°E. This indicates that the monsoon intensity has a great impact

on the diurnal variation of PWV in the TP region. In addition, Liu et al. (2009) pointed out that the extreme values of the diurnal variation of precipitation in most parts of the TP appear during nighttime (16:00–20:00 LST), and the extreme values of the diurnal variation of precipitation in the southern Himalayas appear from night to morning (00:00–04:00 LST). Therefore, it can be concluded that in the southern part of the, the time when the extreme values of the diurnal variation of PWV appear is significantly earlier than that of the diurnal variation of precipitation, while in the central part of the TP, the difference between the diurnal variation of PWV and the diurnal variation of precipitation is not significant, which may be related to the relatively dry conditions in the central part of the plateau and the weak diurnal variation of PWV.

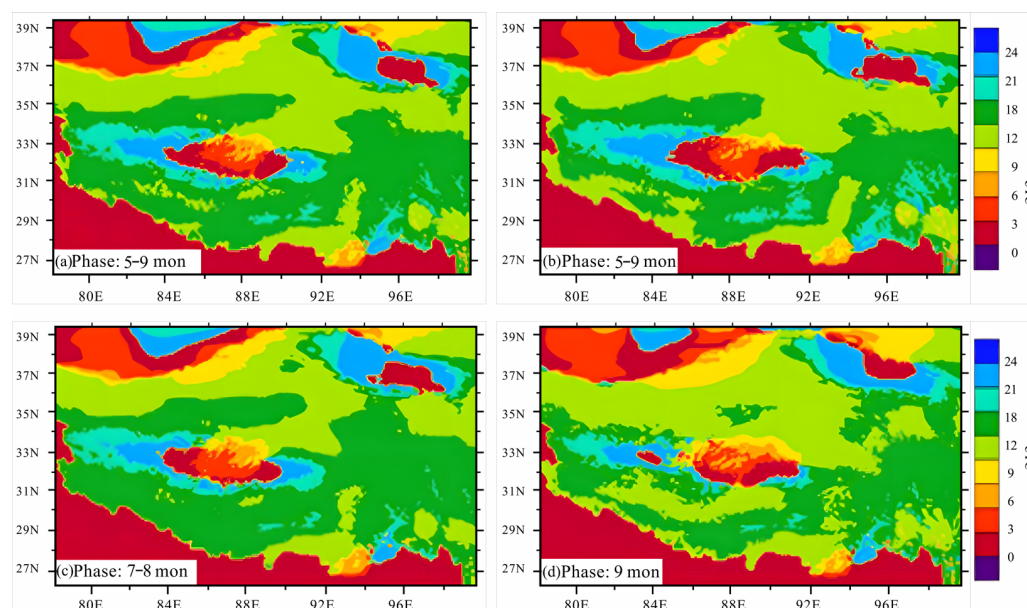


**Figure 4.** Similar to Figure 3, but for the peak time. In panels, (a) May to September; (b) May to June, which is taken as the pre-monsoon period; (c) July to August, the mid-monsoon period; and (d) September, the post-monsoon period.

The clouds and precipitation in the TP exhibit obvious diurnal variations, especially in its southern part, where the amplitude of the diurnal variation is relatively large. Different from the typical diurnal variation on land, the maximum precipitation in the plain area usually occurs between noon and evening, which is caused by the surface heating during the day. However, around the southern slope of the plateau, nocturnal precipitation dominates (Hirose et al., 2008; Ohsawa et al., 2001; Romatschke and Houze, 2011; Sato, 2013; Terao et al., 2006). Kataoka and Saromura (2005) found that the downhill peaks of the nocturnal precipitation peak on the windward slope of the complex mountainous area (Bhatt and Nakamura, 2006; Ohsawa et al., 2001) are the reasons for triggering the maximum precipitation from late night to early morning on the southern slope of the plateau. Sato (2005) emphasized the importance of the nocturnal low-level jet in enhancing the topographic precipitation on the southern slope of the plateau.

## 4. Discussion on Fitting Parameters

### 4.1. Seasonal Variation

The total amount of water vapor in the entire layer is highly dependent on altitude. In many studies, altitude correction for PWV is required. In the altitude correction scheme proposed by Leckner et al. (1978), the altitude-dependent parameter is 0.439. However, due to the high altitude of the TP, in order to further explore the applicability of the empirical

parameter value of altitude correction in the TP, this study not only analyzed it on a temporal scale but also examined its sensitivity to altitude.

As shown in Figure 5a, when performing ANU-SPLIN interpolation with only altitude (H) as the independent covariate, the altitude-dependent parameter of the resulting fitting surface also exhibits certain seasonal variations. The dependence of PWV on altitude in July and August is lower than that in other months, and the parameter values are relatively concentrated. The dependence on altitude in May is slightly higher. During the monsoon period from 2007 to 2015, the absolute value of the parameter ranges from 0.2 to 0.5, with an average value of 0.353.

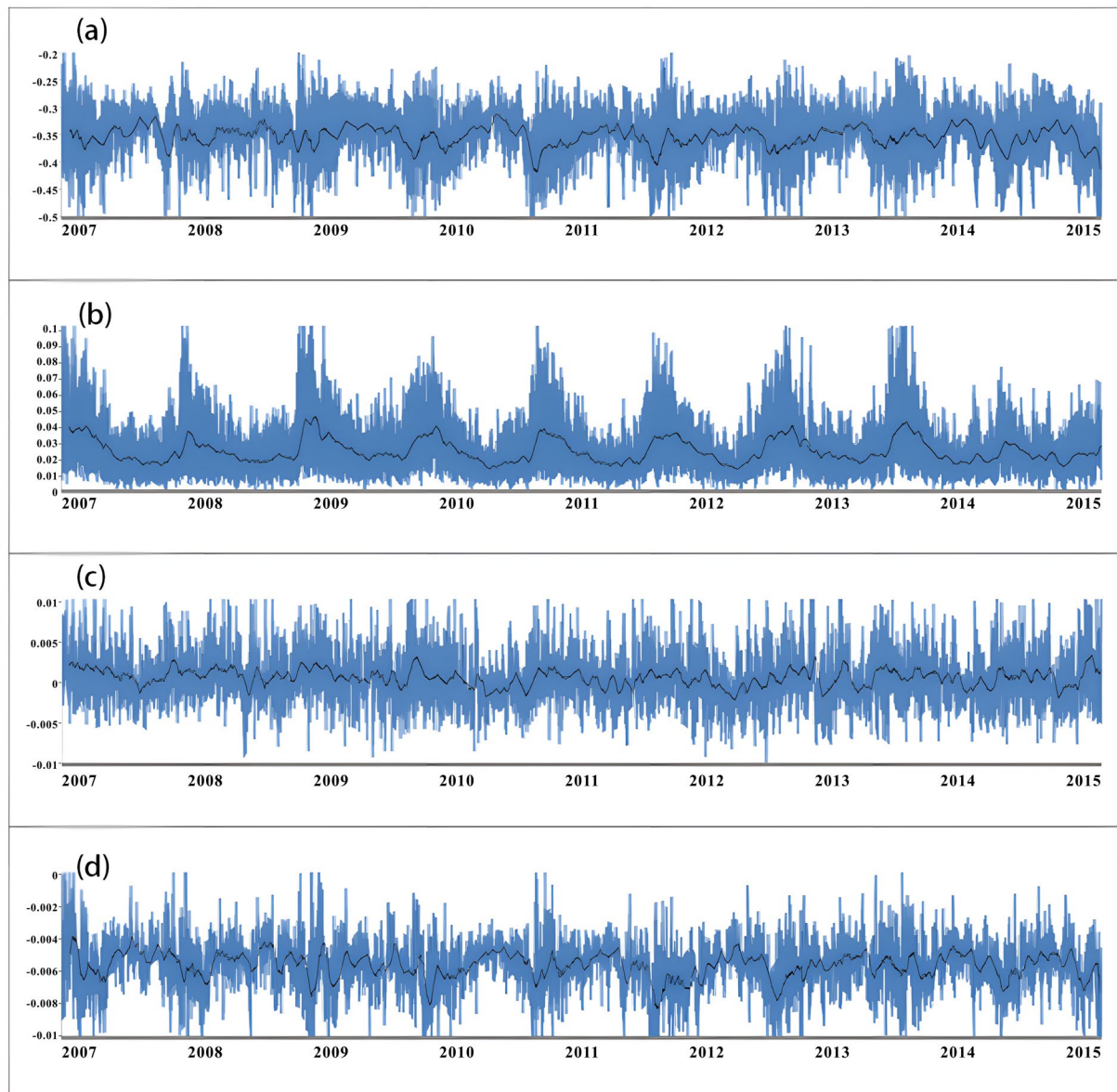


**Figure 5.** Temporal variations of the climate-dependent parameters of the fitting surface during the monsoon period (May–September) from 2007 to 2015: (a) altitude (H), (b) specific humidity (Q), (c) temperature (T), (d) pressure (P).

SPLAIN interpolation with altitude (H), surface air pressure (P), surface air temperature (T), and surface absolute humidity of the atmosphere (Q) as independent covariates was performed, and the temporal variations of the respective resulting parameters are shown in Figure 5. The dependence of PWV on Q and P shows obvious seasonal variations.

Among them, the dependence of PWV on Q is the strongest in May and June and lower in August and September. The dependence of PWV on P is relatively weaker in July and August, and the values of the dependence parameters are more concentrated compared with other months. During the period from May to September 2007–2015, the average value of the dependence parameter of PWV on P was  $-5.67 \times 10^{-3}$ ; the average value of the dependence parameter of PWV on T was  $4.36 \times 10^{-4}$ ; and the average value of the dependence parameter of PWV on Q was  $2.37 \times 10^{-2}$ . Moreover, it can be seen from Figure 5 that PWV decreases with the increase in altitude, increases with the increase in surface humidity, and decreases with the increase in air pressure. However, the correlation with surface air temperature is relatively weak. The dependence parameter of PWV on T ranges from  $-0.01$  to  $0.01$ , with a relatively small average value of  $4.36 \times 10^{-4}$ . This may be caused by the rapid change in surface air temperature. Judging from the magnitudes of the respective parameters, the dependence of PWV on altitude is the strongest, followed by Q and then P, and the weakest is T.

#### 4.2. Elevation Dependence

Based on the MERRA data with hourly resolution within the region of  $26\text{--}40^\circ\text{N}$  and  $78\text{--}100^\circ\text{E}$  in July 2015, the sensitivities of the PWV fitting parameters within different altitude regions, such as 0–8 km, 2–6 km, 3–5 km, 0–1 km, 1–2 km, 2–3 km, 3–4 km, and 4–6 km, were analyzed, as shown in Table 1.

**Table 1.** The dependence parameters of MERRA PWV on covariates in the Qinghai-Tibet Plateau region in July 2015.

	0–8 km	2–6 km	3–5 km	0–1 km	1–2 km	2–3 km	3–4 km	4–6 km
<i>With altitude (H) as the single independent covariate</i>								
H	−0.343	−0.362	−0.376	−2.87	−2.82	−3.06	−3.67	−3.97
<i>With altitude (H), surface air pressure (P), surface air temperature (T), and surface absolute humidity of the atmosphere (Q) as independent covariates.</i>								
H	−0.741	−0.688	−0.504	0.192	−0.813	−0.413	0.409	0.11
P	$-5.12 \times 10^{-3}$	$-4.52 \times 10^{-3}$	$-1.91 \times 10^{-3}$	$4.49 \times 10^{-3}$	$1.57 \times 10^{-3}$	$2.84 \times 10^{-3}$	$4.88 \times 10^{-3}$	$6.90 \times 10^{-3}$
T	$7.03 \times 10^{-4}$	$1.22 \times 10^{-3}$	$1.60 \times 10^{-4}$	$-2.08 \times 10^{-3}$	$4.35 \times 10^{-3}$	$5.16 \times 10^{-3}$	$1.72 \times 10^{-4}$	$2.08 \times 10^{-3}$
Q	$2.03 \times 10^{-2}$	$2.74 \times 10^{-2}$	$2.86 \times 10^{-2}$	$6.55 \times 10^{-3}$	$1.55 \times 10^{-2}$	$3.15 \times 10^{-2}$	$2.93 \times 10^{-2}$	$3.12 \times 10^{-2}$

When other variables remain constant, the dependence of PWV on altitude becomes stronger as altitude increases. Within the height range of 0–2 km, the dependence of PWV on altitude is relatively low, and the absolute value of the parameter is less than 0.3. Since this altitude region is mainly distributed on the southern slope of the Himalayas, where convection is vigorous, and precipitation is abundant, there are also more influencing factors for the total amount of precipitable water in the entire layer. However, above 2 km, from 2 km to 6 km, the absolute value of the dependence parameter of PWV on altitude rises from 3.06 to 3.97. However, it is still lower compared with the parameter in the altitude correction scheme shown in Formula (1). Since the fitting parameters in this section are analyzed based on the months during the monsoon period when the atmospheric moisture is sufficient, PWV is more affected by meso- and micro-scale weather systems than in other seasons. In addition, under the influence of other variables (P, T, and Q), the dependence of PWV on altitude is stronger within the overall region of 0–8 km. The variation of the dependence of PWV on altitude is also relatively large within different altitude regions. Moreover, the dependence of PWV on the surface absolute humidity Q of the atmosphere is one order of magnitude greater than that on the surface air pressure and air temperature, and its variation amplitude with altitude is relatively small. Therefore, in the presence of

humidity variables, humidity-related variables can be incorporated to perform altitude correction on PWV, but the specific fitting formula needs to be determined in further work.

## 5. Summary

Atmospheric water vapor is crucial for rainfall and snowfall, and its diurnal variation affects avalanches. However, in high-altitude mountain areas, vapor product resolution cannot depict this variation well. In this study, the ANUSPLIN was used to obtain  $0.1^\circ \times 0.1^\circ$  2D vapor fields during the 2007–2015 monsoon. Validated against GPS retrievals, the downscaled water vapor field demonstrated higher accuracy and more realistic spatial distributions compared with the original MERRA data. The correlation coefficient improved from 0.71 to 0.88, the bias was significantly reduced from  $-2.24$  to  $0.87$ , and the RMSE decreased from 3.68 to 2.25. In addition, the PWV variation is close to GPS in amplitude and phase in the southern TP. Meanwhile, PWV variation is weak in central TP, strong in other parts, and strongest during mid-monsoon. TP central PWV peaks from night to morning (18:00–4:00 UTC), while southern and northern areas peak from afternoon to evening (8:00–12:00 UTC), 3 h earlier than precipitation. PWV depends most on altitude, then humidity and pressure, and least on surface temperature. It demonstrates some unique characteristics of PWV variation in high-altitude cold mountainous areas, which can serve as a reference for understanding the distinctive patterns of PWV changes in such environments.

**Author Contributions:** Conceptualization, H.L. and Z.H.; methodology, H.L.; software, Z.Q.; validation, H.L.; formal analysis, Z.H.; investigation, H.L.; resources, Z.H.; data curation, H.L.; writing—original draft preparation, H.L.; writing—review and editing, H.L.; visualization, H.L.; supervision, Z.H.; project administration, Z.H.; funding acquisition, Z.H. All authors have read and agreed to the published version of the manuscript.

**Funding:** This research was supported by the Key Science and Technology Program of the Ministry of Emergency Management (No.2024EMST030303) and the Key R&D Program of Tibet Autonomous Region (No. XZ202301ZY0037G).

**Institutional Review Board Statement:** Not applicable.

**Informed Consent Statement:** Not applicable.

**Data Availability Statement:** The original contributions presented in this study are included in the article. Further inquiries can be directed to the corresponding author.

**Conflicts of Interest:** Hongjun Li and Zhuangen Qin are employees of China Anergy Group Third Engineering Bureau Co., Ltd. and Zhengjun Hou is employee of Chengdu Sunvison Intelligent Technology Co., Ltd. The paper reflects the views of the scientists, and not the company.

## References

1. Prasad, A.K.; Singh, R.P. Validation of MODIS Terra, AIRS, NCEP/DOE AMIP-II Reanalysis-2, and AERONET Sun photometer derived integrated precipitable water vapor using ground-based GPS receivers over India. *J. Geophys. Res. Atmos.* **2009**, *114*. [[CrossRef](#)]
2. Shikhovtsev, A.Y.; Kovadlo, P.G.; Khaikin, V.B.; Kiselev, A.V. Precipitable Water Vapor and Fractional Clear Sky Statistics within the Big Telescope Alt-Azimuthal Region. *Remote Sens.* **2022**, *14*, 6221. [[CrossRef](#)]
3. Mancinelli, E.; Passerini, G.; Virgili, S.; Rizza, U. Multi-Decadal Trends in Aerosol Optical Depth of the Main Aerosol Species Based on MERRA-2 Reanalysis: A Case Study in the Baltic Sea Basin. *Remote Sens.* **2024**, *16*, 2421. [[CrossRef](#)]
4. Lu, N.; Qin, J.; Gao, Y.; Yang, K.; Trenberth, K.E.; Gehne, M.; Zhu, Y. Trends and variability in atmospheric precipitable water over the Tibetan Plateau for 2000–2010. *Int. J. Climatol.* **2015**, *35*, 1394–1404. [[CrossRef](#)]
5. Zhao, T.; Wang, J.; Dai, A. Evaluation of atmospheric precipitable water from reanalysis products using homogenized radiosonde observations over China. *J. Geophys. Res. Atmos.* **2015**, *120*, 10,703–10,727. [[CrossRef](#)]

6. Lu, N.; Trenberth, K.E.; Qin, J.; Yang, K.; Yao, L. Detecting Long-Term Trends in Precipitable Water over the Tibetan Plateau by Synthesis of Station and MODIS Observations. *J. Clim.* **2015**, *28*, 1707–1722. [CrossRef]
7. Zhai, P.; Eskridge, R.E. Atmospheric water vapor over China. *J. Clim.* **1997**, *10*, 2643–2652. [CrossRef]
8. Zhou, S.; Wu, P.; Wang, C.; Han, J. Spatial distribution of atmospheric water vapor and its relationship with precipitation in summer over the Tibetan Plateau. *J. Geogr. Sci.* **2012**, *22*, 795–809. [CrossRef]
9. Tian, W.; Tian, H.; Dhomse, S.; Feng, W. A study of upper troposphere and lower stratosphere water vapor above the Tibetan Plateau using AIRS and MLS data. *Atmos. Sci. Lett.* **2011**, *12*, 233–239. [CrossRef]
10. Zhang, Y.; Wang, D.; Zhai, P.; Gu, G.; He, J. Spatial distributions and seasonal variations of tropospheric water vapor content over the Tibetan Plateau. *J. Clim.* **2013**, *26*, 5637–5654. [CrossRef]
11. Lu, N.; Qin, J.; Yang, K.; Gao, Y.; Xu, X.; Koike, T. On the use of GPS measurements for Moderate Resolution Imaging Spectrometer precipitable water vapor evaluation over southern Tibet. *J. Geophys. Res. Atmos.* **2011**, *116*. [CrossRef]
12. Liu, J.; Sun, Z.; Liang, H.; Xu, X.; Wu, P. Precipitable water vapor on the Tibetan Plateau estimated by GPS, water vapor radiometer, radiosonde, and numerical weather prediction analysis and its impact on the radiation budget. *J. Geophys. Res. Atmos.* **2005**, *110*. [CrossRef]
13. Lei, Y.; Yang, K.; Wang, B.; Sheng, Y.; Bird, B.W.; Zhang, G.; Tian, L. Response of inland lake dynamics over the Tibetan Plateau to climate change. *Clim. Change* **2014**, *125*, 281–290. [CrossRef]
14. Shekhar, M.; Chand, H.; Kumar, S.; Srinivasan, K.; Ganju, A. Climate-change studies in the western Himalaya. *Ann. Glaciol.* **2010**, *51*, 105–112. [CrossRef]
15. Duan, A.; Hu, J.; Xiao, Z. The Tibetan Plateau summer monsoon in the CMIP5 simulations. *J. Clim.* **2013**, *26*, 7747–7766. [CrossRef]
16. Yang, K.; Wu, H.; Qin, J.; Lin, C.; Tang, W.; Chen, Y. Recent climate changes over the Tibetan Plateau and their impacts on energy and water cycle: A review. *Glob. Planet. Change* **2014**, *112*, 79–91. Available online: <https://www.sciencedirect.com/science/article/pii/S0921818113002713> (accessed on 25 November 2024). [CrossRef]
17. Xu, X.; Lu, C.; Shi, X.; Gao, S. World water tower: An atmospheric perspective. *Geophys. Res. Lett.* **2008**, *35*. [CrossRef]
18. Yang, K.; Ye, B.; Zhou, D.; Wu, B.; Foken, T.; Qin, J.; Zhou, Z. Response of hydrological cycle to recent climate changes in the Tibetan Plateau. *Clim. Change* **2011**, *109*, 517–534. [CrossRef]
19. Lin, H.; You, Q.; Zhang, Y.; Jiao, Y.; Fraedrich, K. Impact of large-scale circulation on the water vapour balance of the Tibetan Plateau in summer. *Int. J. Climatol.* **2016**, *36*, 4213–4221. [CrossRef]
20. Dai, A.; Wang, J.; Thorne, P.W.; Parker, D.E.; Haimberger, L.; Wang, X.L. A new approach to homogenize daily radiosonde humidity data. *J. Clim.* **2011**, *24*, 965–991. [CrossRef]
21. Dai, A.; Wang, J.; Ware, R.H.; Van Hove, T. Diurnal variation in water vapor over North America and its implications for sampling errors in radiosonde humidity. *J. Geophys. Res. Atmos.* **2002**, *107*, ACL 11-1–ACL 11-14. [CrossRef]
22. Wang, A.; Zeng, X. Evaluation of multireanalysis products with in situ observations over the Tibetan Plateau. *J. Geophys. Res.* **2012**, *117*. [CrossRef]
23. Kuwagata, T.; Numaguti, A.; Endo, N. Diurnal variation of water vapor over the central Tibetan Plateau during summer. *J. Meteorol. Soc. Japan. Ser. II* **2001**, *79*, 401–418. [CrossRef]
24. Xu, X.; Lu, C.; Shi, X.; Ding, Y. Large-scale topography of China: A factor for the seasonal progression of the Meiyu rainband? *J. Geophys. Res. Atmos.* **2010**, *115*. [CrossRef]
25. Liu, J.; Zhu, L.; Zhu, A.X.; Sheng, M.; Duan, Z. Spatial Distribution of Diurnal Rainfall Variation in Summer over China. *J. Hydrometeorol.* **2018**, *19*, 667–678. [CrossRef]
26. Liang, Y.; Yang, B.; Wang, M.; Tang, J.; Sakaguchi, K.; Leung, L.R.; Xu, X. Multiscale Simulation of Precipitation Over East Asia by Variable Resolution CAM-MPAS. *J. Adv. Model. Earth Syst.* **2021**, *13*, e2021MS002656. [CrossRef]
27. Sugimoto, S.; Ueno, K.; Sha, W. Transportation of water vapor into the Tibetan Plateau in the case of a passing synoptic-scale trough. *J. Meteorol. Soc. Jpn.* **2008**, *86*, 935–949. [CrossRef]
28. Letcher, T.W.; Minder, J.R. The simulated response of diurnal mountain winds to regionally enhanced warming caused by the snow albedo feedback. *J. Atmos. Sci.* **2017**, *74*, 49–67. [CrossRef]
29. Gelaro, R.; McCarty, W.; Suárez, M.J.; Todling, R.; Molod, A.; Takacs, L.; Randles, C.A.; Darmenov, A.; Bosilovich, M.G.; Reichle, R. The modern-era retrospective analysis for research and applications, version 2 (MERRA-2). *J. Clim.* **2017**, *30*, 5419–5454. [CrossRef]
30. Wang, Y.; Yang, K.; Pan, Z.; Qin, J.; Chen, D.; Lin, C.; Chen, Y.; Lazhu; Tang, W.; Han, M.; et al. Evaluation of Precipitable Water Vapor from Four Satellite Products and Four Reanalysis Datasets against GPS Measurements on the Southern Tibetan Plateau. *J. Clim.* **2017**, *30*, 5699–5713. [CrossRef]
31. He, J.; Yang, K.; Tang, W.; Lu, H.; Qin, J.; Chen, Y.; Li, X. The first high-resolution meteorological forcing dataset for land process studies over China. *Sci. Data* **2020**, *7*, 25. [CrossRef] [PubMed]
32. Skamarock, W.C.; Klemp, J.B.; Dudhia, J.; Gill, D.O.; Liu, Z.; Berner, J.; Wang, W.; Powers, J.G.; Duda, M.G.; Barker, D.M. A description of the advanced research WRF version 4. *NCAR Tech. Note Ncar/Tn-556+ Str* **2019**, *145*.

33. Panofsky, H.A.; Brier, G.W. *Some Applications of Statistics to Meteorology*; Mineral Industries Extension Services, College of Mineral Industries, Pennsylvania State University: University Park, PA, USA, 1968.
34. Bates, D.M.; Wahba, G. *Computational Methods for Generalized Cross-Validation with Large Data Sets*; University of Wisconsin, Department of Statistics: Madison, WI, USA, 1982.
35. Schimek, M.G. *Smoothing and Regression: Approaches, Computation, and Application*; John Wiley & Sons: Hoboken, NJ, USA, 2013.
36. Zheng, X.; Basher, R. Thin-plate smoothing spline modeling of spatial climate data and its application to mapping South Pacific rainfalls. *Mon. Weather Rev.* **1995**, *123*, 3086–3102. [[CrossRef](#)]
37. Heath, M. GENERALIZED CROSS-VALIDATION AS A METHOD FOR CHOOSING A GOOD RIDGE PARAMETER (WITH M. HEATH AND G. WAHBA). *Milestones in Matrix Computation: The selected works of Gene H. Golub with commentaries: The selected works of Gene H. Golub Comment.* **2007**, *21*, 202.
38. Wahba, G. Smoothing noisy data with spline functions. *Numer. Math.* **1975**, *24*, 383–393. [[CrossRef](#)]

**Disclaimer/Publisher’s Note:** The statements, opinions and data contained in all publications are solely those of the individual author(s) and contributor(s) and not of MDPI and/or the editor(s). MDPI and/or the editor(s) disclaim responsibility for any injury to people or property resulting from any ideas, methods, instructions or products referred to in the content.